


ARTICLE OPEN

Gated tuned superconductivity and phonon softening in monolayer and bilayer MoS₂

Yajun Fu¹, Erfu Liu¹, Hongtao Yuan^{2,3}, Peizhe Tang³, Biao Lian³, Gang Xu³, Junwen Zeng¹, Zhuoyu Chen³, Yaojia Wang¹, Wei Zhou¹, Kang Xu¹, Anyuan Gao¹, Chen Pan¹, Miao Wang¹, Baigeng Wang¹, Shou-Cheng Zhang^{2,3}, Yi Cui^{2,3}, Harold Y. Hwang^{2,3} and Feng Miao¹ 

Superconductors at the atomic two-dimensional limit are the focus of an enduring fascination in the condensed matter community. This is because, with reduced dimensions, the effects of disorders, fluctuations, and correlations in superconductors become particularly prominent at the atomic two-dimensional limit; thus such superconductors provide opportunities to tackle tough theoretical and experimental challenges. Here, based on the observation of ultrathin two-dimensional superconductivity in monolayer and bilayer molybdenum disulfide (MoS₂) with electric-double-layer gating, we found that the critical sheet carrier density required to achieve superconductivity in a monolayer MoS₂ flake can be as low as $0.55 \times 10^{14} \text{ cm}^{-2}$, which is much lower than those values in the bilayer and thicker cases in previous report and also our own observations. Further comparison of the phonon dispersion obtained by ab initio calculations indicated that the phonon softening of the acoustic modes around the M point plays a key role in the gate-induced superconductivity within the Bardeen–Cooper–Schrieffer theory framework. This result might help enrich the understanding of two-dimensional superconductivity with electric-double-layer gating.

npj Quantum Materials (2017)2:52; doi:10.1038/s41535-017-0056-1

INTRODUCTION

Discovery of the interfacial superconducting state at the atomic scale has motivated the pursuit of emergent condensed phases in two-dimensional (2D) electronic systems. Studies of interfacial superconductivity have been generally limited to the regime in which the superconducting order parameter is restricted to 2D. Examples include one-atomic-layer Pb or In films on a Si (111) substrate,^{1–5} single-unit-cell FeSe films on a SrTiO₃ substrate^{6–9} and few layer NbSe₂ crystal.^{10, 11} Recent advances in electric-double-layer (EDL) gating have enabled the continuous tuning of one of the order parameters—the superfluid density—in 2D superconductors on the surface of bulk crystals with unprecedented control of surface band bending, doping level and vortex interaction, thus opening up new opportunities for understanding 2D superconductivity in the surface accumulation layers.^{12–18} With the reduced dimensionality—especially in a strict 2D monolayer form in layered materials in which the disorder, fluctuation and correlation effects all play particularly important roles—being the key parameter, how low the carrier density can be to realize the interfacial superconductivity approaching the ultimate atomic limit remains elusive.

Therefore, to investigate the superconductivity at the monolayer limit starts to be a topic of great interest.¹⁸ As a representative semiconducting layered material, monolayer and bilayer MoS₂ (Fig. 1a) was chosen here as an ideal platform to study superconductivity at its 2D limit because of the following advantages: (1) The dramatic change in the band structure once the crystal is thinned down from bilayer to monolayer provides us

with the possibility to understand the effect of some specific subband structures and Fermi surfaces on the superconductivity; (2) The unique electric-field-driven Zeeman splitting^{16, 19, 20} in the valleys of conduction bands might potentially provide spin-valley locking or a triplet electron pairing mechanism in the unique band structure of monolayer MoS₂,²¹ and (3) Technically, relatively clean atomically thin monolayer and bilayer flakes are easily accessible by using mechanical cleavage. In addition, combined with the powerful accessibility of the EDL gating technique, superconductivity in monolayer and bilayer MoS₂ can help us achieve a deep understanding of the microscopic mechanism of 2D superconductivity. Recently, Costanzo et al.¹⁸ used this technique to study the superconductivity in thin MoS₂ flakes with thickness ranging from mono-layer to six-layers.

In this work, we also demonstrated gate-induced 2D superconductivity in monolayer and bilayer MoS₂ in an electric-double-layer transistor (EDLT) geometry and we found that the monolayer sample showed a smaller critical sheet carrier density requirement to achieve superconductivity than those of bilayer and bulk samples. The comparison studies of their vortex motions on monolayer and bilayer superconductivity were conducted to gain an insight into the differences in the microscopic pictures of the 2D superconductivity. Our further ab initio calculations identified that the superconductivity are mainly induced by the phonon-softening of in-plane acoustic phonon modes and via such a mechanism the monolayer MoS₂ can be more easily driven into superconducting phase with the less electron doping compared to the bilayer case. This work might enrich the understanding of

¹National Laboratory of Solid State Microstructures, School of Physics, Collaborative Innovation Center of Advanced Microstructures, Nanjing University, Nanjing 210093, China;

²Stanford Institute for Materials and Energy Sciences, SLAC National Accelerator Laboratory, Menlo Park, CA 94025, USA and ³Geballe Laboratory for Advanced Materials, Stanford University, Stanford, CA 94305, USA

Correspondence: Hongtao Yuan (htyuan@stanford.edu) or Baigeng Wang (bgwang@nju.edu.cn) or Feng Miao (miao@nju.edu.cn)

Yajun Fu, Erfu Liu, Hongtao Yuan and Peizhe Tang contributed equally to this work

Received: 11 March 2017 Revised: 23 July 2017 Accepted: 7 August 2017

Published online: 12 September 2017

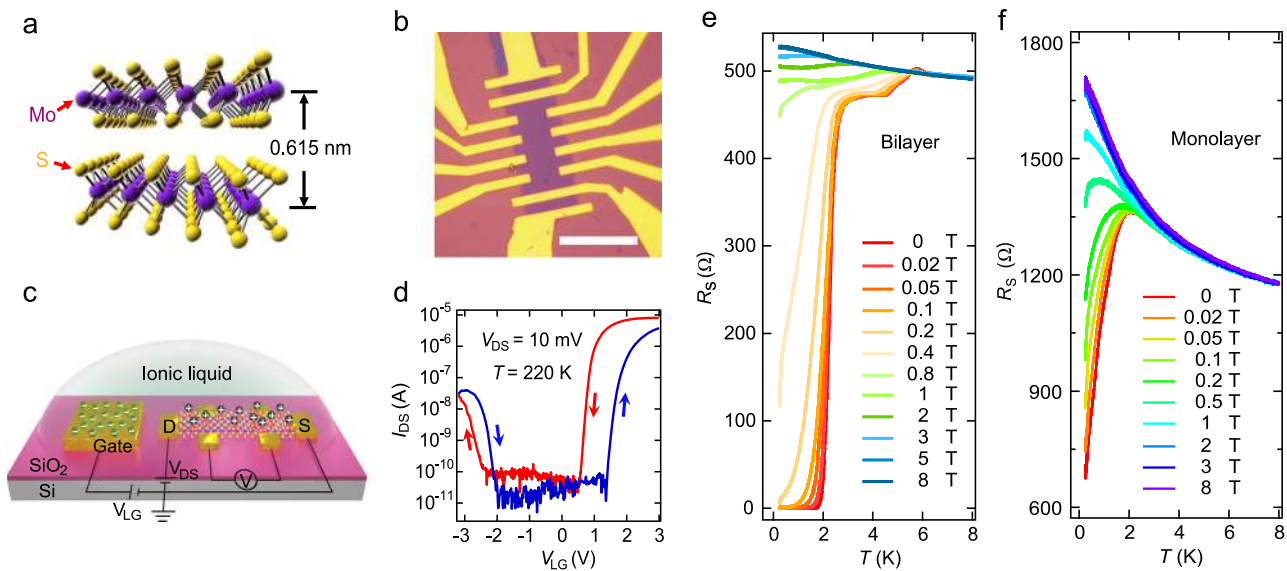


Fig. 1 Crystal structure, device geometry, and gate-induced superconductivity of monolayer and bilayer MoS₂ EDLT devices. **a** Crystal structure of 2H-MoS₂, where the interlayer spacing is 0.615 nm. **b** Optical microscope image of a typical bilayer MoS₂ EDLT device. Scale bar: 20 μm. **c** Schematic illustration of an atomically thin MoS₂ EDLT device. The labels of S and D represent source and drain electrodes, respectively. **d** Typical ambipolar transfer curves obtained from a bilayer MoS₂ EDLT device at 220 K (blue: forward direction; red: backward direction). V_{DS} was fixed at 10 mV. **e, f** T -dependent R_s of bilayer (**e**) and monolayer (**f**) MoS₂ devices at different perpendicular magnetic fields showing gate-induced superconductivity

gated interfacial superconductivity approaching the ultimate atomic limit and provides a method to achieve new types of superconductors.

RESULTS

Figures 1b, c show the typical device structure (optical image) and measurement geometry (schematic illustration) of EDLT using an ionic liquid (DEME-TFSI) as the gate medium. Due to the large tunability of the chemical potential using EDLTs, Fig. 1d presents an ambipolar operation of bilayer MoS₂ EDLT devices at 220 K with an ON-OFF ratio of 10⁵ and a maximum attainable sheet carrier density (n) up to $\sim 2 \times 10^{14} \text{ cm}^{-2}$ by applying sufficiently high gate voltage V_{LG} via the EDL gating medium. As shown in Fig. 1e, in a typical case of a bilayer MoS₂ device with $n = 1.3 \times 10^{14} \text{ cm}^{-2}$ (measured at 10 K), clear superconducting behavior can be observed. The superconducting state was gradually suppressed upon the application of an increasing perpendicular magnetic field and was completely suppressed when the magnetic field reached 1 T (see [supplementary information](#) for more details). In addition to the main drop in sheet resistance R_s at 3.3 K, we noted two other small resistance drops at higher temperatures above the superconducting transition, which are likely caused by the slightly inhomogeneous carrier accumulation. These observations suggest that the inhomogeneity-induced fluctuation in the chemical potential of the channel could cause a more notable effect on the electron transport properties while approaching the 2D limit.

To examine the dimensionality nature of such EDL gating-induced superconductivity, we performed 4-probe voltage-current (V - I) measurements and found that the results satisfied the Berezinskii-Kosterlitz-Thouless (BKT) transition²²⁻²⁴ (supplementary Figs. S3, S4) for 2D superconductivity. The BKT transition corresponds to the spontaneous dissociation of vortex-antivortex pairs into free vortices at the transition temperature T_{BKT} . By fitting the V - I and R_s - T curves, we obtained a transition temperature $T_{BKT} \sim 2 \text{ K}$ (see supplementary Fig. S4 for more details). Compared with thicker MoS₂ devices ($\sim 20 \text{ nm}$),¹⁴ enhancement of back gate

modulation due to the atomically thin geometry was also observed (supplementary Fig. S5).

Superconductivity in a monolayer MoS₂ flake is shown in Fig. 1f. The magnetic field response (shown in Fig. 1f) confirmed that the resistance drop during cooling-down is most likely the superconducting transition. Two remarkable characteristic features must be addressed here. First, before the transition to a superconductor, the resistance of both monolayer and bilayer flakes increases with decreasing temperature (more pronounced in the monolayer case), showing a stronger insulating behavior compared with that observed in thicker MoS₂ flakes (20 nm).¹⁴ This result indicates that disorder plays a more important role in the 2D phase transition while approaching the thin limit. This disorder might originate from the inhomogeneous charge accumulation or the substrate effect on the channels. Second, the critical carrier density required to achieve the superconducting state in the monolayer case is much lower than those values observed in our bilayer case or reported thicker cases,^{14, 16, 20} which we will discuss in detail below. We note that due to the relatively small applied gate voltage to avoid possible electrochemical reactions and the limited temperature accessibility of our equipment, a zero resistance superconducting state was not reached. However, the interface effect between electrodes and sample,^{25, 26} finite-size effects²⁴ and slightly inhomogeneous superconductivity^{15, 27} may also play roles in the non-zero resistance of low dimensional superconductivity. The bilayer superconductivities with zero resistance state under similar conditions suggest that the non-zero resistance case in monolayer MoS₂ cannot be explained by finite-size effects or interface effect between electrodes and sample. The small applied gate voltage and slightly inhomogeneous superconductivity may be possible reasons and will require further investigations.

To study the detailed differences in the critical carrier densities required to achieve superconductivity between monolayer and bilayer MoS₂, we first measured the low-temperature transport properties of bilayer devices at different carrier densities. Figure 2a shows the R_s - T curves ($T = 200$ to 1.6 K) of a different bilayer device (which is different to the one shown in Fig. 1e). With $n = 0.95 \times 10^{14} \text{ cm}^{-2}$ (measured at 10 K with Hall effect results shown

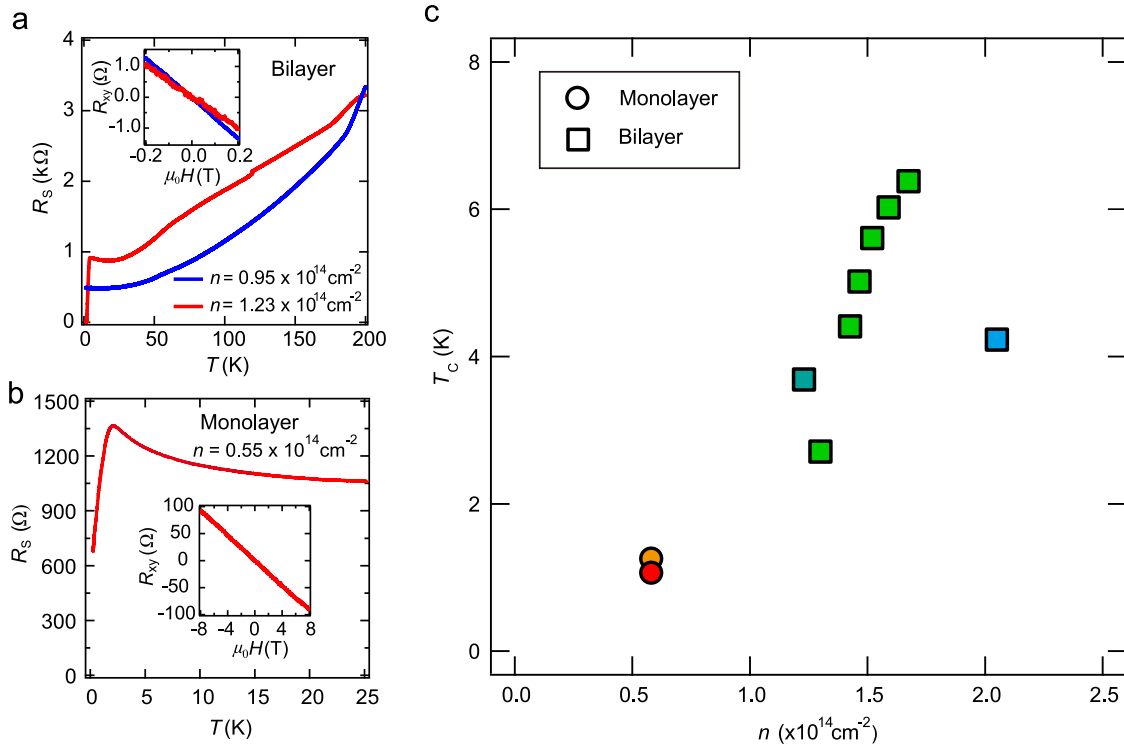


Fig. 2 Comparison of critical carrier densities to achieve superconductivity in monolayer and bilayer MoS₂. **a** Temperature-dependent resistance of a bilayer MoS₂ EDLT at $n = 0.95 \times 10^{14}$ and $1.23 \times 10^{14} \text{ cm}^{-2}$. Inset: Hall measurement results. **b** Temperature-dependent resistance of a monolayer MoS₂ EDLT at $n = 0.55 \times 10^{14} \text{ cm}^{-2}$. Inset: Hall measurement results. **c** Critical temperature T_c versus carrier density n for monolayer and bilayer MoS₂. T_c is defined as $R_s(T_c) = 0.9R_s(10 \text{ K})$

in the inset of Fig. 2a), the device remained metallic until a metal–insulator transition appeared at temperatures down to $\sim 11 \text{ K}$, and no signature of superconductivity was observed. For the same devices, once the sheet carrier density n was increased slightly to $\sim 1.23 \times 10^{14} \text{ cm}^{-2}$, a sharp R_s drop emerged at temperatures of $\sim 4.2 \text{ K}$, and the device reached a zero resistance state at $\sim 1.55 \text{ K}$, indicating the occurrence of superconductivity. For a monolayer MoS₂ device, however, a much smaller critical carrier density ($\sim 0.55 \times 10^{14} \text{ cm}^{-2}$, with the results shown in Fig. 2b) was observed than for those observed in bilayer devices. We summarize the main results in Fig. 2c, where T_c [defined as $R_s(T_c) = 0.9R_s(10 \text{ K})$] is plotted as a function of n for several typical devices (see a similar plot using number of carrier per primitive cell as the standard of the carrier density in Fig. S6, and additional data on homogeneity of carrier densities for multiple pairs of contacts in Fig. S7). All the carrier densities were determined by measuring Hall effect at 10 K , where the monolayer and bilayer MoS₂ maintained normal states. The Hall resistance, R_{xy} , show antisymmetric and linear characteristics when plot as a function of magnetic field (such as the inset of Fig. 2a, b). The negative sign of R_{xy} for positive magnetic field indicate electron-type carriers, which is consistent with the positive gate biases. And the carrier densities were extracted from the Hall coefficient R_H for each gate voltage by using the formula $R_H = 1/ne$. Because disorders or fluctuations are generally believed to play a crucial role in disturbing the superconductivity upon approaching the 2D limit, it is counterintuitive to find that in the ultimate limit case (monolayer), it is “easier” to realize superconductivity than in the bilayer or bulk cases when tuning such a key parameter—carrier density n .

Another approach to gain insight into the differences in the microscopic pictures of the 2D superconductivity in monolayer and bilayer MoS₂ devices is to study their vortex motion.¹⁷ Through analysis of R_s – T plots under various perpendicular

magnetic fields on typical bilayer (Fig. 3a) and monolayer (Fig. 3b) devices, we observed the activated behavior of the vortex dynamics at temperatures slightly lower than T_c and at the resistance saturation at even lower temperatures. This behavior is similar to that recently observed in a ZrNCl EDLT superconductor¹⁷ and in disordered metal thin films.²⁸ At temperatures slightly lower than T_c , the sheet resistance can be described by

$$R_s = R_0(H)e^{-\frac{U(H)}{k_B T}}, \quad (1)$$

where $U(H)$ is the activation energy, and k_B is Boltzmann’s constant. The fitting (black dotted lines in Fig. 3a, b) yields values of $U(H)$. We further plotted the dependence of $U(H)/k_B$ on H , as shown in Fig. 3c, and found that both monolayer and bilayer devices follow the relation of

$$U(H) = U_0 \ln(H_0/H), \quad (2)$$

where $U_0 \sim \Phi_0^2 d / 256\pi^3 \lambda^2$ represents the vortex–antivortex binding energy, Φ_0 is the flux quantum, d is the interlayer spacing, λ is the London penetration length depth, and $H_0 \sim H_{c2}$ (defined as $R_s(H_{c2}) = 0.9R_s(10 \text{ K})$). These results indicate that the vortices in both monolayer and bilayer devices exhibit thermally activated flux flow (TAFF).²⁹ From the fitting results of the bilayer device, we obtained $U_0/k_B = 9.1 \text{ K}$ and $H_0 = 0.37 \text{ T}$ (H_0 was found to be smaller than H_{c2} in this device), which are much larger than those of the monolayer device ($U_0/k_B = 0.12 \text{ K}$ and $H_0 = 0.37 \text{ T}$). At lower temperatures, the resistance deviated from the thermally activated behavior, and a magnetic-field-induced metallic ground state emerged. For the bilayer device, we also measured the magnetic field dependence of R_s at 0.3 K (see [supplementary information](#) for more details) and obtained a good fit (inset of Fig. 3c) by using a model developed by Shimshoni et al.³⁰ and Saito et al.¹⁷ in the low magnetic field regime, indicating that the vortices move through quantum tunneling.

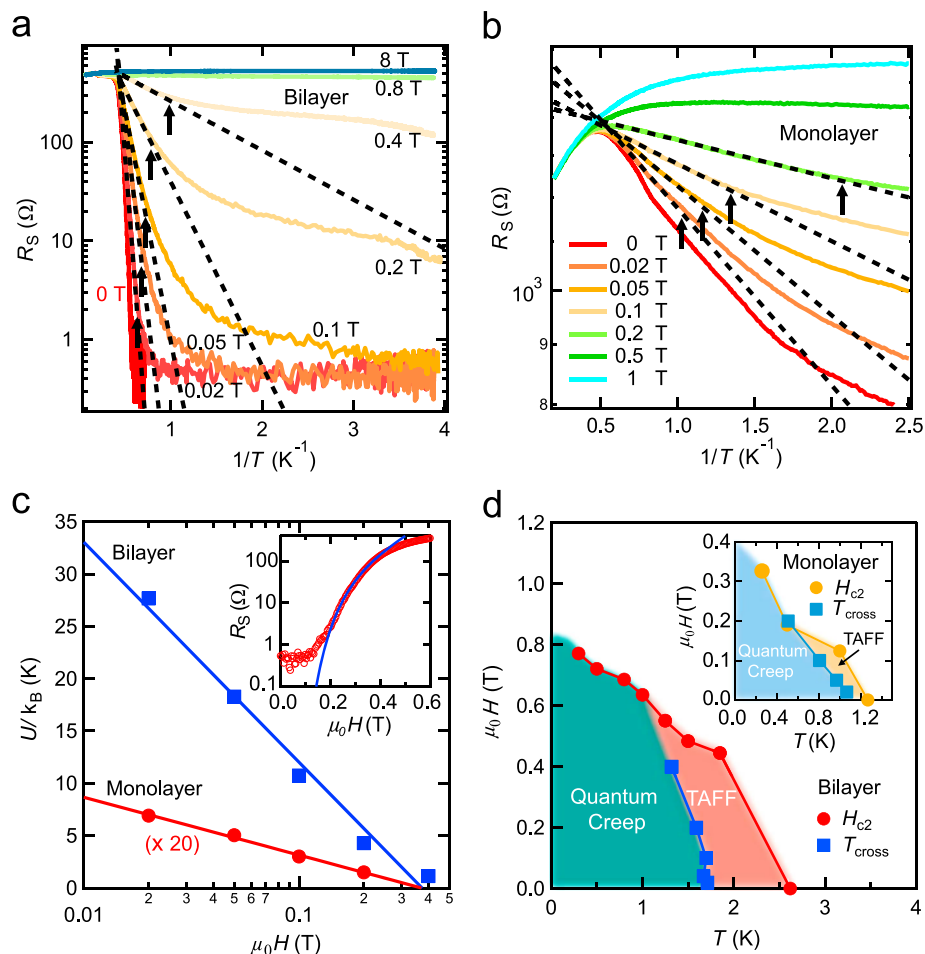


Fig. 3 Vortex dynamics analysis of monolayer and bilayer MoS₂. **a** and **b** show the Arrhenius plot of the sheet resistance of two typical bilayer and monolayer MoS₂ EDLTs at different perpendicular magnetic fields, respectively. The dashed lines show the guide-to-eye fit of the thermally activated behavior, and the arrows show the deviation of the thermally activated regimes. **c** Semilogarithmic plot of the activation energy, $U(H)/k_B$, as a function of magnetic field for both monolayer and bilayer devices. $U(H)/k_B$ data were extracted from fittings in Fig. 3a, b. The solid line is a fit to the formula $U(H) = U_0 \ln(H_0/H)$. Inset: the magnetic field dependence of R_s at 0.3 K with a fit obtained by using a model developed by Shimshoni et al.³⁰ and Saito et al.¹⁷ **d** Vortex phase diagram of the bilayer and monolayer (inset) MoS₂ EDLT devices. The solid circles represent H_{c2} at different temperatures, and the solid squares were extracted from the deviation points as shown in **a** and **b** (depicted by the black arrows). The solid squares divide the thermally activated flux flow (TAFF) and quantum creep regimes

The vortex phase diagrams of both monolayer and bilayer devices based on our observations are plotted in Fig. 3d. Two phases, the TAFF and quantum creep, are confirmed by the measured H_{c2} and thermally activated behavior deviation points. When temperatures drop below T_c , the vortices move through the superconductor by thermal activation, whereas at even lower temperatures in a low magnetic field, vortices move by quantum tunneling. The movement of vortices indicates that even down to atomic thickness, the gate-induced 2D superconductor systems still reside in the weak disorder limit. In gate-induced superconductors in thick flakes of layered materials,¹⁷ the superfluid density is confined in a few layers near the surface, and the 2D superconductors are susceptible only to relatively weak disorder generated by random electric potential from the ions; thus, they exhibit the behavior of a clean 2D superconductor. Herein, the monolayer and bilayer MoS₂ flakes are exfoliated onto SiO₂ wafers, so the 2D superconductor is affected by stronger disorder from the substrate in addition to the ionic liquid. It is worth noting that these systems remain in a regime of a disordered 2D superconductor.

A quantum metallic state was also observed in bilayer NbSe₂ crystal covered by Boron nitride (BN).¹¹ The low temperature resistance of the state fulfills a power-law scaling with magnetic

field, which is consistent with the so-called Bose-metal model. This mainly attributes to the covered BN which protects NbSe₂ crystal from the influence of atmosphere, resulting in a nearly disorder-free condition. While in the case of thin MoS₂ flakes, related EDLT systems remain in the disordered regime where quantum creep is expected to depict the quantum metallic state.¹⁷ This explains why the low temperature resistance of these two systems exhibits different magnetic field dependence. For the quantum metallic state of NbSe₂ systems, it originates from the magnetic field induced strong phase fluctuations. Nevertheless, for the MoS₂ EDLT systems, magnetic-field-induced vortices move through quantum tunneling yields a different metallic ground state. More efforts should be involved to further understand the vortex dynamics of the MoS₂ EDLT systems.

DISCUSSION

To fully understand the physical mechanism of 2D superconducting varying with carrier density, we perform ab initio density functional theory (DFT) calculations for the electronic structures of electron-doped monolayer and bilayer MoS₂. We choose several doping levels (from 0.57×10^{14} to 2.74×10^{14} cm⁻²) to simulate the accumulated carrier density achieved in the liquid gating

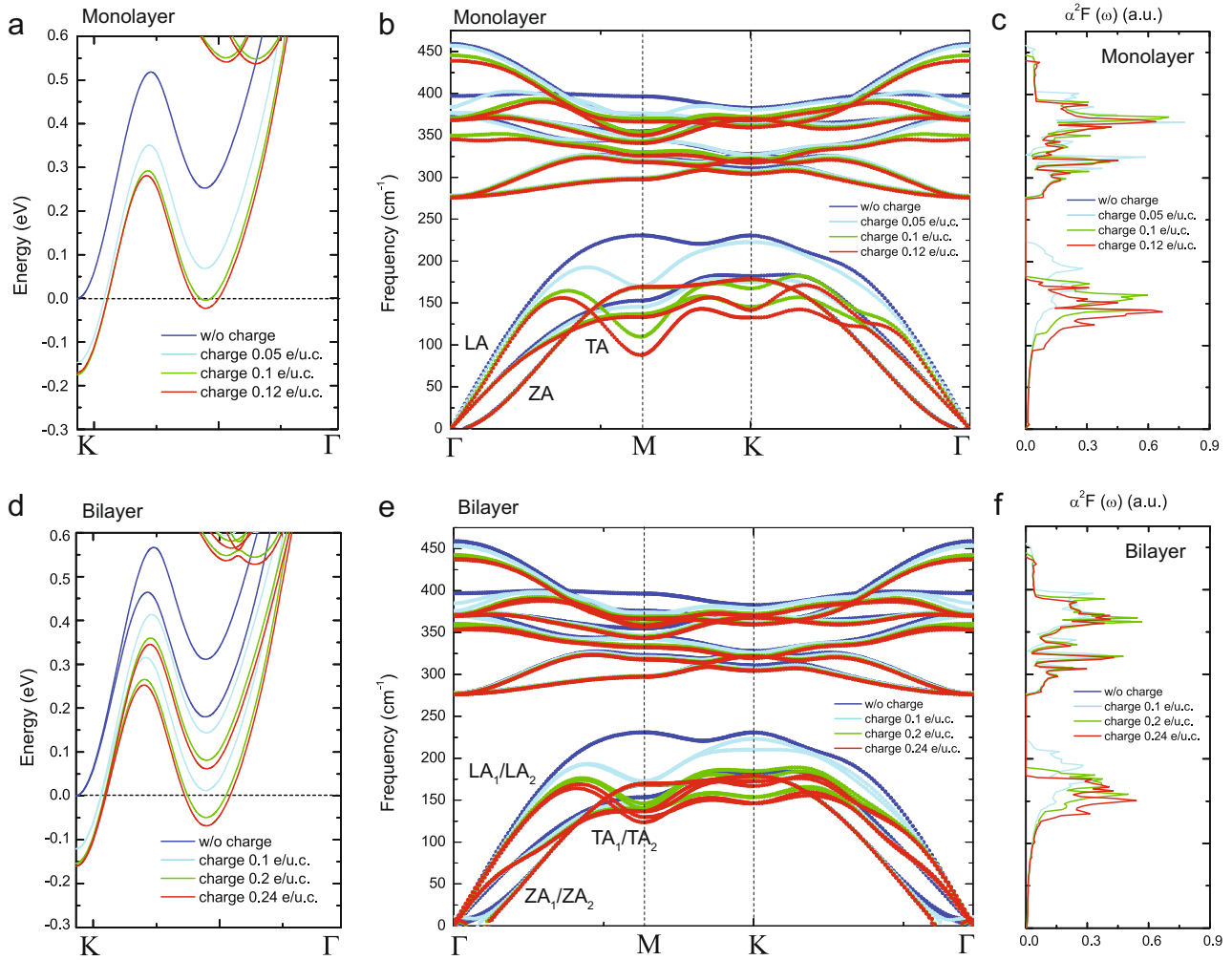


Fig. 4 Calculated electronic structures and electron-phonon couplings for the doped monolayer and bilayer MoS₂. The band structures of **a** monolayer and **d** bilayer MoS₂ with different doping levels. The Fermi level is set to zero and marked by black dotted lines. For the un-doped case, we set the energy of the conduction band minimum to zero. The phonon dispersion and the Eliashberg spectral functional for **b**, **c** monolayer and **e**, **f** bilayer MoS₂ with different doping levels. Herein, LA, TA and ZA stand for in-plane longitudinal mode, in-plane transverse mode and out-plane transverse mode. For bilayer MoS₂, the polarizations of these pairs of acoustic branches are denoted as follows: LA₁/LA₂, TA₁/TA₂ and ZA₁/ZA₂

experiment, which is unavailable for conventional oxide-gated samples. It should be noted here that the electronic band structures of doped monolayer and bilayer MoS₂ strongly depend on the charge doping as shown in Fig. 4a, d. Consistent with previous Angle-resolved photoemission spectroscopy measurement,³¹ the conduction band minima of monolayer and bilayer MoS₂ are always located at the K (K') point even when electrons are injected into the samples. With increasing doping level, the conduction band edge at the K (K') point is filled, and the relative energy difference between the conduction band edge at the K (K') and Λ (Λ') points becomes smaller. By further increasing the electron doping, the states at the Λ (Λ') points are filled, whose energy splitting induced by the spin orbital coupling is much larger than that at the K (K') point.³² Therefore, the electronic Fermi surface of the heavily doped MoS₂ contains two parts: one is around the K and K' points, and the other is located near the Λ and Λ' points. This result directly suggests that the electronic states around the Λ and Λ' points have a greater chance to be paired to form superconducting states via the phonon modes once the carrier density is sufficiently high to induce superconductivity in this system (as discussed below), which is different from previous reports.²⁰

In the framework of Bardeen–Cooper–Schrieffer theory, the superconducting T_c is mainly determined by the electron–phonon coupling,³³ the averaged coupling constant has the expression of

$$\lambda = 2 \int d\omega \frac{\alpha^2 F(\omega)}{\omega} = \sum_{\mathbf{q}, \nu} \frac{2\gamma_{\mathbf{q}, \nu}}{\hbar N(\epsilon_F) \omega_{\mathbf{q}, \nu}^2}, \quad (3)$$

where $\alpha^2 F(\omega)$ is the Eliashberg spectral functional, $N(\epsilon_F)$ is the electronic density of states at the Fermi level, $\omega_{\mathbf{q}, \nu}$ is the phonon frequency, and $\gamma_{\mathbf{q}, \nu}$ is the phonon line width (see the Methods section). Thus, herein, by using density functional perturbation theory (DFPT),³⁴ we calculated the phonon bands and electron-phonon coupling for monolayer MoS₂ with different doping levels as shown in Fig. 4b, c. Toward the low-frequency part of the acoustic phonons that mainly contributes to superconductivity, the phonon softening of longitudinal and transverse acoustic phonon modes (LA and TA modes) is found around the M point with low carrier density (blue line in Fig. 4b); with increasing electron doping, the LA and TA modes can be further softened around the K point. This effect occurs because the electronic states around the Λ (Λ') point are filled at higher doping levels. However, for the whole calculated doping range, the out-of-plane mode (ZA mode), $N(\epsilon_F)$ and $\gamma_{\mathbf{q}, \nu}$ change little (see [supplementary](#)

information for more details). Thus, we conclude that the gate-induced superconductivity for the doped monolayer MoS₂ originates from the phonon softening of low-frequency TA and LA modes at the K and M points, and this result is further confirmed by the $\alpha^2F(\omega)$ calculations (see Fig. 4c).

In contrast to monolayer MoS₂ superconductivity, the accumulated carrier density of a doped bilayer is lower for the same magnitude of T_c , which is observed experimentally in Fig. 2c. These phenomena are confirmed by our DFPT calculations. In Fig. 4e, f, we show the calculated phonon dispersions and electron–phonon couplings for doped bilayer MoS₂. It is found that although the phonon softening also occurs at the M and K (K') points, the magnitude is much weaker in bilayer MoS₂ at the same doping level, which indicates that superconductivity in the bilayer or multilayer MoS₂ is more difficult to achieve due to the interlayer coupling. In experimental reality, the influence of the substrate and fluctuations in and inhomogeneity of the electron distribution also play important roles for 2D superconducting, which is still an open question and cannot be captured by our DFT calculations.

In conclusion, we demonstrate that in the gate-induced 2D superconductivity of both monolayer and bilayer MoS₂ flakes, the monolayer sample has an apparently smaller critical sheet carrier density to achieve superconductivity than those of bilayer and bulk samples. The ab initio calculation results point to the phonon softening of in-plane acoustic phonon modes as a possible origin of these observations. Our work paves the way for further understanding of gated interfacial superconductivity approaching the ultimate atomic limit and pursuing a new type of superconductor.

METHODS

Materials and devices

The monolayer and bilayer MoS₂ flakes on silicon wafers (covered by 300-nm-thick SiO₂) were fabricated by standard mechanical exfoliation of bulk MoS₂ (SPI supplies). The number of layers was determined by measuring the thickness of the flakes using a Bruker Multimode 8 atomic force microscope or performing micro Raman scattering (Horiba-JY T64000) measurements (under ambient conditions in the backscattering geometry with an incident laser wavelength of 514.5 nm). A conventional electron-beam lithography process (FEI F50 with an NPGS pattern generation system) followed by standard electron-beam evaporation of metal electrodes (typically 5 nm Ag/ 40 nm Au) was used to fabricate Hall bar electrodes.

Transport measurements

The ionic liquid used in this study was *N,N*-diethyl-*N*-(2-methoxyethyl)-*N*-methylammonium bis-(trifluoromethylsulfonyl)-imide (DEME-TFSI). An ionic liquid drop was applied onto MoS₂ devices with Hall geometry and covered both the MoS₂ flake and a side gate electrode to form an EDLT. Before any electrical measurements were performed, the MoS₂ EDLT devices were stored under a vacuum better than 10^{−2} mbar and cooled down to 220 K to avoid possible interfacial chemical reactions.

The transport measurements of all MoS₂ EDLTs were performed in an Oxford Instruments Teslatron™ CF cryostat. Due to the freezing of the ionic liquid at low temperatures, we applied different values of V_{LG} to accumulate carriers of certain density at 220 K and cooled down with a fixed V_{LG} . A lock-in amplifier (Stanford Research 830) was used to measure the 4-probe resistance through the AC approach.

Ab initio calculations

The ab initio calculations were performed by using DFT as implemented in the Quantum Espresso³⁵ package. For the electronic structure calculations, the 32 × 32 × 1 Monkhorst-Pack k points were used with the generalized gradient approximation (GGA) functional³⁶ and norm-conserving pseudopotential. To correctly describe the electronic structures of monolayer and bilayer MoS₂ and repeat the previous calculations,³¹ the in-plane lattice constant was chosen as 3.18 Å; the vacuum layer was chosen as 15 Å that was sufficiently large to avoid the interaction between adjacent layers, and

inner coordinates of unit-cell were fully relaxed. Phonon band structures and electron–phonon couplings were calculated within DEPT³⁴ based on the evaluation of the dynamical matrices on the 8 × 8 × 1 q -mesh. For the phonon dispersion, SOC was not considered.

Data availability

The data that support the findings of this study are available from the corresponding author upon reasonable request.

ACKNOWLEDGEMENTS

This work was supported in part by the National Key Basic Research Program of China (2015CB921600, 2013CBA01603), the National Natural Science Foundation of China (11374142, 61574076), the Natural Science Foundation of Jiangsu Province (BK20130544, BK20140017, BK20150055), the Specialized Research Fund for the Doctoral Program of Higher Education (20130091120040), and Fundamental Research Funds for the Central Universities and the Collaborative Innovation Center of Advanced Microstructures. This work was partially supported by the Department of Energy, Office of Basic Energy Sciences, Division of Materials Sciences and Engineering, under contract DE-AC02-76SF00515. P.Z.T., B.L., G.X. and S.C.Z. also acknowledge NSF under grant number DMR-1305677.

AUTHOR CONTRIBUTIONS

Y.J. F., E.F. L., H.T. Y. and P.Z. T. contributed equally to this work. F. M. and H.T. Y. conceived the project and designed the experiments. Y.J. F., E.F. L., J.W. Z., Y.J. W., W. Z., K. X., A.Y. G., C. P., and M. W. performed device fabrication, characterization and transport measurements. Y.J. F., E.F. L., F. M. and H.T. Y. performed data analysis and interpretation. P.Z. T., B. L., X. G., Z.Y. C. and S.C. Z. performed DFT calculations. H.T. Y., F. M., Y.J. F. and E.F. L. co-wrote the paper, and all authors contributed to the discussion and preparation of the manuscript.

ADDITIONAL INFORMATION

Supplementary Information accompanies the paper on the *npj Quantum Materials* website (doi:10.1038/s41535-017-0056-1).

Competing interests: The authors declare that they have no competing financial interests.

Publisher's note: Springer Nature remains neutral with regard to jurisdictional claims in published maps and institutional affiliations.

REFERENCES

- Qin, S., Kim, J., Niu, Q. & Shih, C. Superconductivity at the two-dimensional limit. *Science* **324**, 1314–1317 (2009).
- Zhang, T. et al. Superconductivity in one-atomic-layer metal films grown on Si (111). *Nat. Phys.* **6**, 104–108 (2010).
- Uchihashi, T., Mishra, P., Aono, M. & Nakayama, T. Macroscopic superconducting current through a silicon surface reconstruction with indium adatoms: Si(111) $-(\sqrt{7} \times \sqrt{3})$ -In. *Phys. Rev. Lett.* **107**, 207001 (2011).
- Yamada, M., Hirahara, T. & Hasegawa, S. Magnetoresistance measurements of a superconducting surface state of In-induced and Pb-induced structures on Si (111). *Phys. Rev. Lett.* **110**, 237001 (2013).
- Brun, C. et al. Remarkable effects of disorder on superconductivity of single atomic layers of lead on silicon. *Nat. Phys.* **10**, 444–450 (2014).
- Liu, D. et al. Electronic origin of high-temperature superconductivity in single-layer FeSe superconductor. *Nat. Commun.* **3**, 931 (2012).
- He, S. et al. Phase diagram and electronic indication of high-temperature superconductivity at 65 K in single-layer FeSe films. *Nat. Mater.* **12**, 605–610 (2013).
- Lee, J. J. et al. Interfacial mode coupling as the origin of the enhancement of T_c in FeSe films on SrTiO₃. *Nature* **515**, 245–248 (2014).
- Liu, X. et al. Dichotomy of the electronic structure and superconductivity between single-layer and double-layer FeSe/SrTiO₃ films. *Nat. Commun.* **5**, 5047 (2014).
- Xi, X. et al. Ising pairing in superconducting NbSe₂ atomic layers. *Nat. Phys.* **12**, 139–143 (2016).
- Tsen, A. W. et al. Nature of the quantum metal in a two-dimensional crystalline superconductor. *Nat. Phys.* **12**, 208–212 (2016).
- Ye, J. T. et al. Liquid-gated interface superconductivity on an atomically flat film. *Nat. Mater.* **9**, 125–128 (2009).

13. Ueno, K. et al. Discovery of superconductivity in KTaO_3 by electrostatic carrier doping. *Nat. Nanotechnol.* **6**, 408–412 (2011).
14. Ye, J. T. et al. Superconducting dome in a gate-tuned band insulator. *Science* **338**, 1193–1196 (2012).
15. Taniguchi, K., Matsumoto, A., Shimotani, H. & Takagi, H. Electric-field-induced superconductivity at 9.4 K in a layered transition metal disulfide MoS_2 . *Appl. Phys. Lett.* **101**, 042603 (2012).
16. Lu, J. M. et al. Evidence for two-dimensional Ising superconductivity in gated MoS_2 . *Science* **350**, 1353–1357 (2015).
17. Saito, Y., Kasahara, Y., Ye, J. T., Iwasa, Y. & Nojima, T. Metallic ground state in an ion-gated two-dimensional superconductor. *Science* **350**, 409–413 (2015).
18. Costanzo, D., Jo, S., Berger, H. & Morpurgo, A. F. Gate-induced superconductivity in atomically thin MoS_2 crystals. *Nat. Nanotechnol.* **11**, 339–344 (2016).
19. Yuan, H. T. et al. Zeeman-type spin splitting controlled by an electric field. *Nat. Phys.* **9**, 563–569 (2013).
20. Saito, Y. et al. Superconductivity protected by spin-valley locking in ion-gated MoS_2 . *Nat. Phys.* **12**, 144–149 (2016).
21. Yuan, N. F., Mak, K. F. & Law, K. T. Possible topological superconducting phases of MoS_2 . *Phys. Rev. Lett.* **113**, 097001 (2014).
22. Halperin, B. I. & Nelson, D. R. Resistive transition in superconducting films. *J. Low Temp. Phys.* **36**, 599–616 (1979).
23. Minnhagen, P. The two-dimensional Coulomb gas, vortex unbinding, and superfluid-superconducting films. *Rev. Mod. Phys.* **59**, 1001–1066 (1987).
24. Benfatto, L., Castellani, C. & Giamarchi, T. Broadening of the Berezinskii-Kosterlitz-Thouless superconducting transition by inhomogeneity and finite-size effects. *Phys. Rev. B* **80**, 214506 (2009).
25. Wang, J. et al. Superconductivity in single crystalline Pb nanowires contacted by normal metal electrodes. *Phys. Rev. B* **86**, 035439 (2012).
26. Tian, M. L., Wang, J., Ning, W., Mallouk, T. E. & Chan, M. H. W. Surface superconductivity in thin cylindrical Bi nanowire. *Nano. Lett.* **15**, 1487–1492 (2015).
27. Jo, S., Costanzo, D., Berger, H. & Morpurgo, A. F. Electrostatically induced superconductivity at the surface of WS_2 . *Nano. Lett.* **15**, 1197–1202 (2015).
28. Ephron, D., Yazdani, A., Kapitulnik, A. & Beasley, M. R. Observation of quantum dissipation in the vortex state of a highly disordered superconducting thin film. *Phys. Rev. Lett.* **76**, 1529–1532 (1996).
29. Feigel'Man, M. V., Geshkenbein, V. B. & Larkin, A. I. Pinning and creep in layered superconductors. *Physica C Supercond.* **167**, 177–187 (1990).
30. Shimshoni, E., Auerbach, A. & Kapitulnik, A. Transport through quantum melts. *Phys. Rev. Lett.* **80**, 3352–3355 (1998).
31. Yuan, H. T. et al. Evolution of the valley position in bulk transition-metal chalcogenides and their monolayer limit. *Nano. Lett.* **16**, 4738–4745 (2016).
32. Molina-Sánchez, A., Sangalli, D., Hummer, K., Marini, A. & Wirtz, L. Effect of spin-orbit interaction on the optical spectra of single-layer, double-layer, and bulk MoS_2 . *Phys. Rev. B* **88**, 045412 (2013).
33. Bardeen, J., Cooper, L. N. & Schrieffer, J. R. Theory of superconductivity. *Phys. Rev.* **108**, 1175–1204 (1957).
34. Baroni, S., De Gironcoli, S., Dal Corso, A. & Giannozzi, P. Phonons and related crystal properties from density-functional perturbation theory. *Rev. Mod. Phys.* **73**, 515–562 (2001).
35. Giannozzi, P. et al. QUANTUM ESPRESSO: a modular and open-source software project for quantum simulations of materials. *J. Phys. Condens. Matter.* **21**, 395502 (2009).
36. Perdew, J. P., Burke, K. & Ernzerhof, M. Generalized gradient approximation made simple. *Phys. Rev. Lett.* **77**, 3865–3868 (1996).



Open Access This article is licensed under a Creative Commons Attribution 4.0 International License, which permits use, sharing, adaptation, distribution and reproduction in any medium or format, as long as you give appropriate credit to the original author(s) and the source, provide a link to the Creative Commons license, and indicate if changes were made. The images or other third party material in this article are included in the article's Creative Commons license, unless indicated otherwise in a credit line to the material. If material is not included in the article's Creative Commons license and your intended use is not permitted by statutory regulation or exceeds the permitted use, you will need to obtain permission directly from the copyright holder. To view a copy of this license, visit <http://creativecommons.org/licenses/by/4.0/>.

© The Author(s) 2017